

Discovery of High Dimensional Band Topology in Twisted Bilayer Graphene

Chao Ma^{1#}, Qiyue Wang^{2#}, Scott Mills³, Xiaolong Chen¹, Bingchen Deng¹, Shaofan Yuan¹,
Cheng Li¹, Kenji Watanabe⁴, Takashi Taniguchi⁴, Du Xu^{3*}, Fan Zhang^{2*}, and Fengnian Xia^{1*}

¹*Department of Electrical Engineering, Yale University, New Haven, Connecticut 06511, USA*

²*Department of Physics, The University of Texas at Dallas, Richardson, TX 7508, USA*

³*Department of Physics and Astronomy, Stony Brook University, Stony Brook, NY 11794, USA*

⁴*National Institute for Materials Science, 1-1 Namiki, Tsukuba 305-0044, Japan*

Abstract:

Recently twisted bilayer graphene (t-BLG)¹⁻⁵ emerges as a new strongly correlated physical platform near a magic twist angle⁴, which hosts many exciting phenomena such as the Mott-like insulating and unconventional superconducting behavior⁶⁻¹⁰. Besides the apparent significance of band flatness⁴, band topology may be another critical element in strongly correlated twistrionics yet receives much less attention¹¹⁻¹⁴. Here we report the discovery of nontrivial high dimensional band topology in t-BLG moiré bands through a systematic nonlocal transport study^{15, 16}, in conjunction with an examination rooted in K -theory¹⁷. The moiré band topology of t-BLG manifests itself as two pronounced nonlocal responses in the electron and hole superlattice gaps. We further show that the nonlocal responses are robust to the interlayer electric field, twist angle, and edge termination, exhibiting a universal scaling law. While an unusual symmetry of t-BLG trivializes Berry curvature, we elucidate that two high dimensional Z_2 invariants characterize the topology of the moiré Dirac bands, validating the topological origin of the observed nonlocal responses. Our findings not only provide a new perspective for understanding the emerging strongly correlated phenomena in twisted van der Waals heterostructures, but also suggest a potential strategy to achieve topologically nontrivial metamaterials from topologically trivial quantum materials based on twist engineering.

These authors contribute equally to this work.

fengnian.xia@yale.edu; zhang@utdallas.edu; xu.du@stonybrook.edu;

It is widely known that overlaying two identical periodic lattices with a relative twist generates a larger-scale interference structure, i.e., the moiré pattern. For two-dimensional (2D) materials, such twists create moiré superlattices by reducing translation symmetry in real space and folds electron Bloch bands into moiré Brillouin zones (MBZ) in momentum space¹⁻⁵. The moiré bands can exhibit striking phenomena such as the Hofstadter's butterfly in fractal quantum Hall effect¹⁸⁻²⁰ and the moiré potential-modulated interlayer excitons²¹⁻²⁴. Remarkably, strongly correlated electron behavior including Mott-like insulating phases and possibly unconventional superconductivity have been discovered in twisted bilayer graphene⁶⁻⁹ (t-BLG) near a magic angle⁴ ($\sim 1.1^\circ$) and in aligned trilayer graphene/hexagonal boron nitride (hBN) heterostructures^{25, 26}. Besides their extreme band flatness, nontrivial band topology may be another crucial feature in determining the observed strongly correlated phases. One celebrated example is the well-studied incompressible fractional quantum Hall effect¹¹, in which the partially filled Landau level has a nontrivial Chern number¹². Another example is the predicted Z_4 parafermions¹³, for which the 8π Josephson effect is mediated by a helical edge state of 2D topological insulator (TI)¹⁴ with a sufficiently small velocity. Therefore, it is of significance to investigate the possible topology of the active moiré bands in these correlated systems, which however has yet to be demonstrated experimentally, despite the most recent tantalizing discussions relating the t-BLG band topology to the concept of wannierizability²⁷⁻²⁹.

Here we experimentally reveal the universal and unique moiré band topology of t-BLG at small twist angles by using systematic nonlocal transport measurements^{15, 16, 30-32}. Previously, a nonlocal measurement scheme has been employed in detecting the helical edge state of 2D TI¹⁵ and the topological valley current driven by Berry curvature^{16, 30-32}. In this work, pronounced nonlocal responses are observed in both the electron and hole superlattice gaps of t-BLG³³ and persist in a wide range of applied displacement fields from 0 to 0.62 V/nm. Moreover, the nonlocal responses are consistently observed in 15 t-BLG devices with twist angles between $\sim 1.3^\circ$ and $\sim 1.9^\circ$, showing their robustness to twist angle and edge termination. We elucidate that the unique $C_{2z}T$ symmetry of t-BLG, though trivializing any Berry curvature, gives rise to two nontrivial bulk Z_2 invariants that previously appear in six and seven dimensions in the celebrated periodic table of topological classification¹⁷. While one invariant protects the moiré Dirac points, the other dictates

the presence of one pair of counter-propagating edge states per spin-valley in each superlattice gap. We further show that the observed non quantization and universal scaling of nonlocal resistance are consistent with the $C_{2z}T$ and valley symmetry breaking at edges. Our findings not only unveil the appealing moiré band topology of t-BLG but also offer a universal pathway for creating topological metamaterials by twist engineering 2D materials. The discovered moiré band topology may provide a new perspective for deciphering the tantalizing strongly correlated phenomena⁶⁻¹⁰ in magic-angle t-BLG.

A schematic of our typical t-BLG devices is shown in Fig. 1a. We employed a “tear-and-stack” technique to fabricate hBN encapsulated t-BLG heterostructures as reported previously^{5, 33, 34} (Methods). A Hall-bar geometry was defined through reactive ion etching, and electrical contacts to t-BLG were made at the edge³⁴. The total carrier concentration n in t-BLG, estimated based on a capacitor model, is controlled by tuning the voltage applied to the global silicon back gate. The schemes of local and nonlocal measurements are illustrated in the lower inset in Fig. 1b. We first characterize the t-BLG moiré superlattice by measuring the four-probe local resistance R_L as a function of n at 80 K in a device (D1) shown in the top inset in Fig. 1b. (See Extended Data Fig. 1a for the complete temperature dependence of R_L down to 10 K.)

Three resistance maxima are observed at the charge neutrality point and at $n = \pm n_s \approx 6.50 \times 10^{12} \text{cm}^{-2}$ (Fig. 1b), at which the Fermi level crosses the degenerate Dirac points from the two original graphene monolayers and the two moiré superlattice-induced band gaps due to the interlayer hybridizations³³, respectively. Here, n_s denotes the carrier concentration corresponding to 4 electrons per moiré unit cell³³, from which we can deduce the twist angle of this device to be $\sim 1.68^\circ$. The error is estimated to be around $\pm 0.05^\circ$. Figure 1c shows the calculated moiré band structure of 1.68° t-BLG (Methods), where the red region in the middle and the two white regions adjacent to it highlight the two moiré Dirac bands (per spin-valley) and the two superlattice gaps, respectively. Both of the superlattice gaps are extracted to be ~ 40 meV based on the temperature dependent transport measurements (Extended Data Fig. 1b), which is slightly larger than the calculated gaps (Fig. 1c). Strikingly, pronounced nonlocal responses $R_{NL} = V/I$ are observed in

the superlattice gaps on both the electron- and hole-sides, as featured in Fig. 1b. The peaks of R_{NL} have a narrower range in n compared with that of R_L and attenuate to zero away from $\pm n_s$.

We first exclude the possibility from stray current-induced Ohmic nonlocal resistance, which can be estimated by the van der Pauw relation^{16, 35-38} $R_{NL,Ohmic} = R_L w / \pi L \exp(-\pi L / w)$. Here $L = 3 \mu m$ is the channel length between the driving and probing terminals and $w = 1.2 \mu m$ is the channel width. The Ohmic contribution only yields $R_{NL,Ohmic} < 1 \Omega$ at the superlattice gaps, which is at least two orders of magnitude smaller than our observed R_{NL} peak values. With lowering the temperature to 1.7 K, R_{NL} continues to grow and exhibits fluctuations without any obvious quantization (Extended Data Fig. 2). While excluding the presence of protected gapless edge states¹⁵, our observation is reminiscent of the nonlocal transport driven by valence-band Berry curvatures³⁹ in several 2D materials^{16, 30-32}. However, Berry curvature vanishes in t-BLG. The C_{2z} rotational symmetry requires the Berry curvatures of opposite momenta to be the same, whereas the time-reversal (T) symmetry requires them to be opposite. Thus, the $C_{2z}T$ symmetry of t-BLG leaves any momentum invariant and dictates any Berry curvature to be zero.

Because $(C_{2z}T)H(\mathbf{k})(C_{2z}T)^{-1} = H(\mathbf{k})$ and $(C_{2z}T)^2 = 1$, t-BLG Hamiltonian $H(\mathbf{k})$ belongs to class AI in the celebrated periodic table of topological classification rooted in K -theory¹⁷. In this classification (Table 1), the topological invariant of $H(\mathbf{k})$ is determined by $d-D$, where d (D) denotes the number of dimensions in which momentum is odd (even) under $C_{2z}T$. Evidently, t-BLG can be characterized by two independent Z_2 invariants, as $H(\mathbf{k})$ is featured by $d=0$ and $D=1$ or 2. We find that both invariants are nontrivial for the moiré Dirac bands of t-BLG (per spin-valley). One Z_2 invariant ($d-D=7$ in Table 1) amounts to the quantized Berry phase (0 or π) of the lower band along a loop in the MBZ. The π Berry phase ensures the presence of Dirac points at K_s or K_s' in the MBZ, which is confirmed by our observation of minimum conductivity at the charge neutrality below ~ 60 K (Extended Data Fig. 1a) and previous measurements by other groups^{33, 40}.

$(d-D) \bmod 8$	0	1	2	3	4	5	6	7
Invariant	Z	0	0	0	$2Z$	0	Z_2	Z_2

Table 1. Topological classification¹⁷ for class AI in the Altland-Zirnbauer table. The cases with $d = 0$ and $D = 1, 2$ are relevant for the moiré Dirac bands of t-BLG. Because of the unique $C_{2z}T$ symmetry, the nontrivial Z_2 index of $d-D = 7$ protects each bulk Dirac point, and the nontrivial Z_2 index of $d-D = 6$ (Fig. 1e) leads to the (gapped) counter-propagating edge states in each superlattice gap (Fig. 1f).

The other Z_2 invariant ($d-D=6$ in Table 1) over the entire MBZ can be visualized by computing the Wilson loop spectral flow⁴¹ of the two moiré Dirac bands. This spectral flow corresponds to a wannier-center counterflow (calculated by using circle 1 in Fig. 1d) along a loop (circle 2 in Fig. 1d) around the MBZ (torus in Fig. 1d), and the Z_2 invariant characterizes the parity of the counterflow winding. In Fig. 1e, the red traces illustrate the counterflow winding for the two moiré Dirac bands, and the two crossings are symmetry-enforced stable points (Methods). Consistent topological features have also been discussed²⁷⁻²⁹, based on different and complicated approaches. The nontrivial counterflow, reminiscent of that of 2D TI⁴¹, implies the presence of a pair of counter-propagating edge states per spin-valley in the electron superlattice gap (dashed curves in Fig. 1f). Because of the particle-hole symmetry evidenced in Fig. 1c, such edge states also exist in the hole superlattice gap. Yet, due to the breaking of $C_{2z}T$ and valley symmetries by t-BLG boundary, the edge states acquire gaps (solid curves in Fig. 1f). This is consistent with our observation of non-quantized nonlocal responses at low temperatures; the spreading of edge states into the bulk forms quasi-one-dimensional diffusion channels.

Next, we examine the impact of interlayer electric field on the discovered nonlocal response. To independently control the total carrier concentration n and the average displacement field D , we fabricated a dual-gate t-BLG device (D2). In this device (inset in Fig. 2a), by tuning the top (V_{TG}) and bottom (V_{BG}) gate biases, we achieve $n = -(C_{TG}(V_{TG} - V_{TG,0}) + C_{BG}(V_{BG} - V_{BG,0}))/e$ and $D = (-C_{TG}(V_{TG} - V_{TG,0}) + C_{BG}(V_{BG} - V_{BG,0}))/2\varepsilon_0$ based on a parallel-capacitor model⁴². Here ε_0 is the vacuum permittivity, e is the electron charge, C_{TG} (C_{BG}) is the capacitance of top (back)

gate-dielectric layer, and $V_{TG,0}$ ($V_{BG,0}$) is the offset voltage due to unintentional doping. In Fig. 2a we show the local resistance R_L mapping as a function of both V_{TG} and V_{BG} at 80 K. The two superlattice gaps manifest as the resistance maxima along the constant doping lines $n = \pm n_s$. As $|D|$ changes from 0 to 0.62 V/nm, R_L at n_s ($-n_s$) varies by a factor of ~ 1.5 (2.5). The moderate change in R_L implies that the superlattice gaps are not closed by the applied D fields. Consistently, the calculated moiré bands do not exhibit any qualitative change for an interlayer potential difference of 100 meV (Extended Data Fig. 3).

Importantly, as shown in Fig. 2b, appreciable nonlocal responses are observed at $n = \pm n_s$ no matter whether or not the D field vanishes. (R_{NL} drops dramatically to zero away from $\pm n_s$.) Not only is this consistent with the fact that the D field does not break the $C_{2z}T$ symmetry, it also validates that the origin of nonlocal responses in t-BLG is distinct from the electric field driven Berry curvatures in other 2D materials^{30, 31}. On the electron side, the R_{NL} peak decreases from ~ 1.4 to ~ 0.9 k Ω as D reduces from 0.62 to 0.02 V/nm (Fig. 2b). We attribute the moderate enhancement in R_{NL} with D to the possible formation of network of AB-BA domain wall modes⁴³⁻⁴⁵ under D fields. Such a conducting network has been imaged in t-BLG⁴⁶⁻⁴⁸ and may contribute to the nonlocal transport. The nonlocal responses on the hole side exhibit a relatively complex dependence on D for $D < 0$. Sharp negative R_{NL} peaks appear on the higher concentration side as D increases from -0.3 V/nm to 0. (See Methods for detailed discussions on the hole-side R_{NL} .) The imperfect particle-hole symmetry of t-BLG may explain the observed asymmetric D dependence of R_{NL} on the electron and hole sides. Nevertheless, similar particle-hole asymmetry has also been noticed in other t-BLG studies⁷⁻¹⁰.

We now extend our nonlocal measurements to t-BLG of different twist angles. We observe that the nonlocal responses are universal in all our t-BLG devices with twist angles from $\sim 1.3^\circ$ to $\sim 1.9^\circ$. Figure 3 denotes the nonlocal measurement results from Devices 3 to 7. (See Extended Data Table 1 for the device details.) For each twist angle, the red curve plots the measured R_{NL} data recorded at 80 K, whereas the blue curve plots the calculated density of states (DOS) as a function of carrier concentration n (Methods). For each twist angle, the pronounced R_{NL} peaks coincide well with the

DOS minima, which correspond to the two superlattice gaps separating the moiré Dirac bands in t-BLG spectra. We emphasize that the moiré Dirac bands of our studied small-angle t-BLG are topologically equivalent since the superlattice gaps do not close as the twist angle decrease from $\sim 2^\circ$ to the magic angle $\sim 1.1^\circ$ (Methods and Extended Data Fig. 3). Thus, our observation above the magic angle reveals unambiguously the nontrivial band topology of the moiré Dirac bands as a whole near the magic angle. Moreover, the standard etching process (Methods) defined arbitrary edge terminations in our devices. Thus, the existence of strong nonlocal responses in all our t-BLG devices implies the robustness of the observed phenomenon against the edge termination.

To further elaborate the physical mechanism of the observed nonlocal responses, we measure the length dependence of R_{NL} in a multi-terminal Hall bar device (D8) at 80 K. From the local resistance measurement, we estimate that the twisted angle is $\sim 1.89^\circ$. Figure 4a displays three set of R_{NL} data obtained by choosing three channels with different driving and/or probing terminal pairs, as illustrated by the device micrograph in the upper inset in Fig. 4a. We notice that the peak positions of different channels are slightly off aligned, which is likely due to the charge inhomogeneity in the sample. Quantitatively, the R_{NL} peak values exponentially decay with the channel length L (lower inset in Fig. 4a), and the linear fitting in the semi-log plot yields characteristic diffusion lengths $\lambda_e \approx 1.2 \mu\text{m}$ and $\lambda_h \approx 1.4 \mu\text{m}$ for the electron- and hole-side, respectively.

The scaling between R_{NL} and R_L is essential to understand the nonlocal transport mechanism. A power-law relation $R_{NL} \sim R_L^\alpha$ is revealed by the Arrhenius plot (Fig. 4b) for the data points around $R_{NL}(R_L)$ peaks in the range $n \pm \Delta n = -5.54 \pm 0.28$ and 5.54 ± 0.22 (10^{12}cm^{-2}) measured in a 1.54° t-BLG device (D9). The fitting parameter α is found to be 3.00 (2.51), 3.37 (2.36), 3.01 (2.17) and 3.50 (2.29) for hole-side (electron-side) responses at 80, 90, 100, and 110 K, respectively. This power-law scaling, together with the above revealed diffusion behavior, suggests that $R_{NL} \sim R_L^\alpha e^{-L/\lambda}$. Furthermore, the magnitude of R_{NL} peaks on both electron and hole sides are reduced by ~ 100 times from 80 to 180 K (Fig. 4c). At room temperature, the nonlocal responses can no longer be clearly identified. From the semi-log plot of R_{NL} peak versus I/T (inset

in Fig. 4c), it is clear that R_{NL} has similar thermal activation behavior as R_L in the superlattice gaps. The activation energies E_{NL} (E_L) are extracted to be 157 ± 20 meV (36 ± 1 meV) and 129 ± 16 meV (34 ± 2 meV) for the electron and hole sides, respectively, with $E_{NL}/E_L \sim 4$. We attribute this deviation from α to the temperature dependence of λ , since stronger scattering at higher temperature reduces λ and effectively enhances E_{NL}/E_L .

The observed scaling relation between R_{NL} and R_L in t-BLG is rather unusual. Previously, similar behavior is suggested for the spin Hall effect⁴⁹ and seen for the valley Hall effects^{16, 30-32}, where the nonlocal transport is captured by a cubic law $R_{NL} \sim R_L^3 \sigma_{xy}^{v,s} e^{-L/\lambda^{v,s}} / \lambda^{v,s}$. Here $\sigma_{xy}^{v,s}$ and $\lambda^{v,s}$ refer to the valley (spin) Hall conductivity and the valley (spin) diffusion length, respectively. In t-BLG, the symmetry-trivialized Berry curvature and negligibly weak spin-orbit coupling imply vanishing $\sigma_{xy}^{v,s}$. However, the spreading of gapped edge states into the bulk forms quasi-one-dimensional diffusion channels and support the nonlocal transport over $1 \mu\text{m}$ at 80 K. Future measurements through scanning tunneling microscope^{40, 48}, scanning superconducting quantum interference^{50, 51}, and microwave impedance microscopy⁵² may directly image such edge channels in the t-BLG superlattice gaps. Nevertheless, the robustness of observed nonlocal signatures against the interlayer electric field, twist angle, and edge termination not only provides compelling evidence for the nontrivial band topology of t-BLG but also may open a new avenue for creating, engineering, and exploiting moiré quantum information by twistronics and nonlocal means.

Acknowledgements: The work at Yale University is partially supported by the National Science Foundation EFRI NewLAW Program and the Office of Naval Research Young Investigator Program (ONR-YIP). The theoretical works (QW and FZ) are supported by Army Research Office (ARO) under Grant Number W911NF-18-1-0416. FZ is grateful to Fengcheng Wu and Adrian Po for valuable discussions. K.W. and T.T. acknowledge support from the Elemental Strategy Initiative conducted by the MEXT, Japan and the CREST (JPMJCR15F3), JST.

Figure captions

Figure 1 | Signature of band topology in small-twist-angle bilayer graphene. **a**, Schematic of a typical single-gate device with t-BLG channel. The carrier concentration n is tuned by a global silicon back gate. Inset: Schematic moiré pattern of t-BLG consisting two layers of monolayer graphene with a twist. **b**, Local and nonlocal resistances measured in a t-BLG device (D1) with a 1.68° twist angle at 80 K. The three resistance maxima of local resistance correspond to the Dirac points (at charge neutrality) and the superlattice bandgaps (at $n = \pm n_s \approx \pm 6.50 \times 10^{12} \text{ cm}^{-2}$). Pronounced nonlocal responses are observed inside the superlattice bandgaps. Inset: Optical image of a t-BLG device (D1). Scale bar: $4 \mu\text{m}$. **c**, The calculated moiré band structure of 1.68° t-BLG. Two moiré Dirac bands appear in the red shaded region. **d**, Schematic torus illustrating the first moiré Brillouin zone. Two wannier centers of the two moiré Dirac bands along circle 1 are computed, and their counterflow along circle 2 is depicted in **e**. **e**, Two red traces illustrating the nontrivial wannier-center counterflow winding, and the crossings labeled by 0 and π are symmetry-enforced stable points. **f**, Illustration of the counter-propagating edge states per spin-valley (dashed curves) in the superlattice bandgaps. The edge states acquire gaps (solid curves) due to symmetry breaking at t-BLG boundaries.

Figure 2 | Displacement field dependence of local and nonlocal resistances. **a**, Local resistance map as a function of V_{BG} and V_{TG} . Inset: Optical image of dual-gate device (D2) with a scale bar of $4 \mu\text{m}$. **b**, Nonlocal resistance measured as a function of V_{BG} and V_{TG} . The gray dashed lines denote several different displacement fields. Pronounced nonlocal responses are observed at around the two superlattice bandgaps at $n = \pm n_s$. All data were taken from D2 at 80 K.

Figure 3 | Twist angle dependence of nonlocal resistance and DOS. Measured nonlocal resistance (red curves) and calculated density of states (DOS) as functions of n measured in various t-BLG devices (D3 to D7) with different twist angles from $\sim 1.3^\circ$ to $\sim 1.9^\circ$ at 80 K. (See Extended Table 1 for device details.) Nonlocal resistance peaks appear at the DOS minima corresponding to the superlattice bandgaps in each t-BLG.

Figure 4 | Length and temperature dependence of nonlocal resistance. **a**, Length dependence of nonlocal responses in a multiterminal device (D8) measured at 80 K. Three sets of R_{NL} are measured by driving current I and probing voltage drop V using different pairs of terminals as indicated in the figure legend. Top left inset: Optical image of D8. Scale bar: $3 \mu\text{m}$. Middle inset:

Semi-log plot of R_{NL} peaks versus channel length L . The nonlocal responses exponentially decay with L . Solid points and circles represent the electron- and hole-side R_{NL} peak values, respectively. The fittings (dashed lines) yield diffusion lengths of 1.2 and 1.4 μm for electron and hole sides, respectively. **b**, Scaling relation between R_{NL} and R_L measured in D9 at different temperatures. Data points around the R_{NL} (R_L) peaks are extracted in the range $n \pm \Delta n = 5.54 \pm 0.22$ and -5.54 ± 0.28 (10^{12}cm^{-2}) for the electron (orange shaded region) and hole (green shaded region) sides. A linear relation between $\ln R_{NL}$ and $\ln R_L$ gives a slope 3.00 (2.51), 3.37 (2.36), 3.01 (2.17) and 3.50 (2.29) for hole-side (electron-side) responses at 80, 90, 100, and 110 K, respectively. **c**, Temperature dependence of R_{NL} from 80 K up to room temperature. Inset: Semi-log plot of R_{NL} peak values versus $100/T$. Above 80 K, R_{NL} also exhibits thermal activation behavior with the activation energies extracted to be 157 ± 20 meV and 129 ± 16 meV for the electron and hole sides, respectively.

References

1. Rong, Z.Y. & Kuiper, P. Electronic effects in scanning tunneling microscopy: moiré pattern on a graphite surface. *Phys. Rev. B* **48**, 17427-17431 (1993).
2. Lopes dos Santos, J.M.B., Peres, N.M.R. & Castro Neto, A.H. Graphene bilayer with a twist: electronic structure. *Phys. Rev. Lett.* **99**, 256802 (2007).
3. Mele, E.J. Commensuration and interlayer coherence in twisted bilayer graphene. *Phys. Rev. B* **81**, 161405 (2010).
4. Bistritzer, R. & MacDonald, A.H. Moiré bands in twisted double-layer graphene. *Proc. Natl Acad. Sci. USA* **108**, 12233-12237 (2011).
5. Kim, K. et al. Van der Waals heterostructures with high accuracy rotational alignment. *Nano Lett.* **16**, 1989-1995 (2016).
6. Cao, Y. et al. Correlated insulator behaviour at half-filling in magic-angle graphene superlattices. *Nature* **556**, 80–84 (2018).
7. Cao, Y. et al. Unconventional superconductivity in magic-angle graphene superlattices. *Nature* **556**, 43–50 (2018).
8. Yankowitz, M. et al. Tuning superconductivity in twisted bilayer graphene. *Science* **363**, 1059-1064 (2019).

9. Codecido, E. et al. Correlated insulating and superconducting states in twisted bilayer graphene below the magic angle. *arXiv preprint arXiv:1902.05151* (2019).
10. Sharpe, A.L. et al. Emergent ferromagnetism near three-quarters filling in twisted bilayer graphene. *arXiv preprint arXiv:1901.03520* (2019).
11. Laughlin, R.B. Anomalous quantum Hall effect: an incompressible quantum fluid with fractionally charged excitations. *Phys. Rev. Lett.* **50**, 1395-1398 (1983).
12. Thouless, D.J., Kohmoto, M., Nightingale, M.P. & den Nijs, M. Quantized Hall conductance in a two-dimensional periodic potential. *Phys. Rev. Lett.* **49**, 405-408 (1982).
13. Zhang, F. & Kane, C.L. Time-reversal-invariant Z_4 fractional Josephson effect. *Phys. Rev. Lett.* **113**, 036401 (2014).
14. Kane, C.L. & Mele, E.J. Z_2 topological order and the quantum spin Hall effect. *Phys. Rev. Lett.* **95**, 146802 (2005).
15. Roth, A. et al. Nonlocal transport in the quantum spin Hall state. *Science* **325**, 294-297 (2009).
16. Gorbachev, R.V. et al. Detecting topological currents in graphene superlattices. *Science* **346**, 448-451 (2014).
17. Teo, J.C.Y. & Kane, C.L. Topological defects and gapless modes in insulators and superconductors. *Phys. Rev. B* **82**, 115120 (2010).
18. Hunt, B. et al. Massive Dirac fermions and Hofstadter butterfly in a van der Waals heterostructure. *Science* **340**, 1427-1430 (2013).
19. Dean, C.R. et al. Hofstadter's butterfly and the fractal quantum Hall effect in moiré superlattices. *Nature* **497**, 598–602 (2013).
20. Ponomarenko, L.A. et al. Cloning of Dirac fermions in graphene superlattices. *Nature* **497**, 594–597 (2013).
21. Seyler, K.L. et al. Signatures of moiré-trapped valley excitons in $\text{MoSe}_2/\text{WSe}_2$ heterobilayers. *Nature* **567**, 66-70 (2019).
22. Jin, C. et al. Observation of moiré excitons in WSe_2/WS_2 heterostructure superlattices. *Nature* **567**, 76-80 (2019).
23. Tran, K. et al. Evidence for moiré excitons in van der Waals heterostructures. *Nature* **567**, 71-75 (2019).

24. Alexeev, E.M. et al. Resonantly hybridized excitons in moiré superlattices in van der Waals heterostructures. *Nature* **567**, 81-86 (2019).
25. Chen, G. et al. Evidence of a gate-tunable Mott insulator in a trilayer graphene moiré superlattice. *Nature Physics* **15**, 237-241 (2019).
26. Chen, G. et al. Signatures of gate-tunable superconductivity in trilayer graphene/boron nitride moiré superlattice. *arXiv preprint arXiv:1901.04621* (2019).
27. Song, Z. et al. All "magic angles" are "stable" topological. *arXiv preprint arXiv:1807.10676* (2018).
28. Po, H.C., Zou, L., Senthil, T. & Vishwanath, A. Faithful tight-binding models and fragile topology of magic-angle bilayer graphene. *arXiv preprint arXiv:1808.02482* (2018).
29. Ahn, J., Park, S. & Yang, B.-J. Failure of Nielsen-Ninomiya theorem and fragile topology in two-dimensional systems with space-time inversion symmetry: application to twisted bilayer graphene at magic angle. *arXiv preprint arXiv:1808.05375* (2018).
30. Sui, M. et al. Gate-tunable topological valley transport in bilayer graphene. *Nat. Phys.* **11**, 1027–1031 (2015).
31. Shimazaki, Y. et al. Generation and detection of pure valley current by electrically induced Berry curvature in bilayer graphene. *Nat. Phys.* **11**, 1032–1036 (2015).
32. Wu, Z. et al. Intrinsic valley Hall transport in atomically thin MoS₂. *Nature Commun.* **10**, 611 (2019).
33. Cao, Y. et al. Superlattice-induced insulating states and valley-protected orbits in twisted bilayer graphene. *Phys. Rev. Lett.* **117**, 116804 (2016).
34. Wang, L. et al. One-dimensional electrical contact to a two-dimensional material. *Science* **342**, 614-617 (2013).
35. Brüne, C. et al. Evidence for the ballistic intrinsic spin Hall effect in HgTe nanostructures. *Nat. Phys.* **6**, 448–454 (2010).
36. Abanin, D.A. et al. Giant nonlocality near the Dirac point in graphene. *Science* **332**, 328-330 (2011).
37. Balakrishnan, J., Kok Wai Koon, G., Jaiswal, M., Castro Neto, A.H. & Özyilmaz, B. Colossal enhancement of spin–orbit coupling in weakly hydrogenated graphene. *Nat. Phys.* **9**, 284-287 (2013).

38. Mishchenko, A. et al. Nonlocal response and anamorphosis: the case of few-layer black phosphorus. *Nano Lett.* **15**, 6991-6995 (2015).
39. Zhang, F. Brought to light. *Nat. Phys.* **14**, 111–113 (2017).
40. Kim, K. et al. Tunable moiré bands and strong correlations in small-twist-angle bilayer graphene. *Proc. Natl Acad. Sci. USA* **114**, 3364-3369 (2017).
41. Yu, R., Qi, X.L., Bernevig, A., Fang, Z. & Dai, X. Equivalent expression of Z_2 topological invariant for band insulators using the non-Abelian Berry connection. *Phys. Rev. B* **84**, 075119 (2011).
42. Zhang, Y. et al. Direct observation of a widely tunable bandgap in bilayer graphene. *Nature* **459**, 820–823 (2009).
43. Zhang, F., MacDonald, A.H. & Mele, E.J. Valley Chern numbers and boundary modes in gapped bilayer graphene. *Proc. Natl Acad. Sci. USA* **110**, 10546-10551 (2013).
44. Vaezi, A., Liang, Y., Ngai, D.H., Yang, L. & Kim, E.-A. Topological edge states at a tilt boundary in gated multilayer graphene. *Phys. Rev. X* **3**, 021018 (2013).
45. Ju, L. et al. Topological valley transport at bilayer graphene domain walls. *Nature* **520**, 650–655 (2015).
46. Jiang, L. et al. Soliton-dependent plasmon reflection at bilayer graphene domain walls. *Nat. Mater.* **15**, 840–844 (2016).
47. Sunku, S.S. et al. Photonic crystals for nano-light in moiré graphene superlattices. *Science* **362**, 1153-1156 (2018).
48. Huang, S. et al. Topologically protected helical states in minimally twisted bilayer graphene. *Phys. Rev. Lett.* **121**, 037702 (2018).
49. Abanin, D.A., Shytov, A.V., Levitov, L.S. & Halperin, B.I. Nonlocal charge transport mediated by spin diffusion in the spin Hall effect regime. *Phys. Rev. B* **79**, 035304 (2009).
50. Nowack, K.C. et al. Imaging currents in HgTe quantum wells in the quantum spin Hall regime. *Nat. Mater.* **12**, 787–791 (2013).
51. Spanton, E.M. et al. Images of Edge Current in InAs/GaSb quantum wells. *Phys. Rev. Lett.* **113**, 026804 (2014).
52. Shi, Y. et al. Imaging quantum spin Hall edges in monolayer WTe₂. *Sci. Adv.* **5**, eaat8799 (2019).

- 53. Chung, T.-F., Xu, Y. & Chen, Y.P. Transport measurements in twisted bilayer graphene: Electron-phonon coupling and Landau level crossing. *Phys. Rev. B* **98**, 035425 (2018).
- 54. Koshino, M. et al. Maximally localized wannier orbitals and the extended Hubbard model for twisted bilayer graphene. *Phys. Rev. X* **8**, 031087 (2018).
- 55. Zhang, F., Jung, J., Fiete, G.A., Niu, Q. & MacDonald, A.H. Spontaneous quantum Hall states in chirally stacked few-layer graphene systems. *Phys. Rev. Lett.* **106**, 156801 (2011).
- 56. Bouhon, A., Black-Schaffer, A.M. & Slager, R.-J. Wilson loop approach to topological crystalline insulators with time reversal symmetry. *arXiv preprint arXiv:1804.09719* (2018).

Figure 1: Signature of band topology in small-twist-angle bilayer graphene

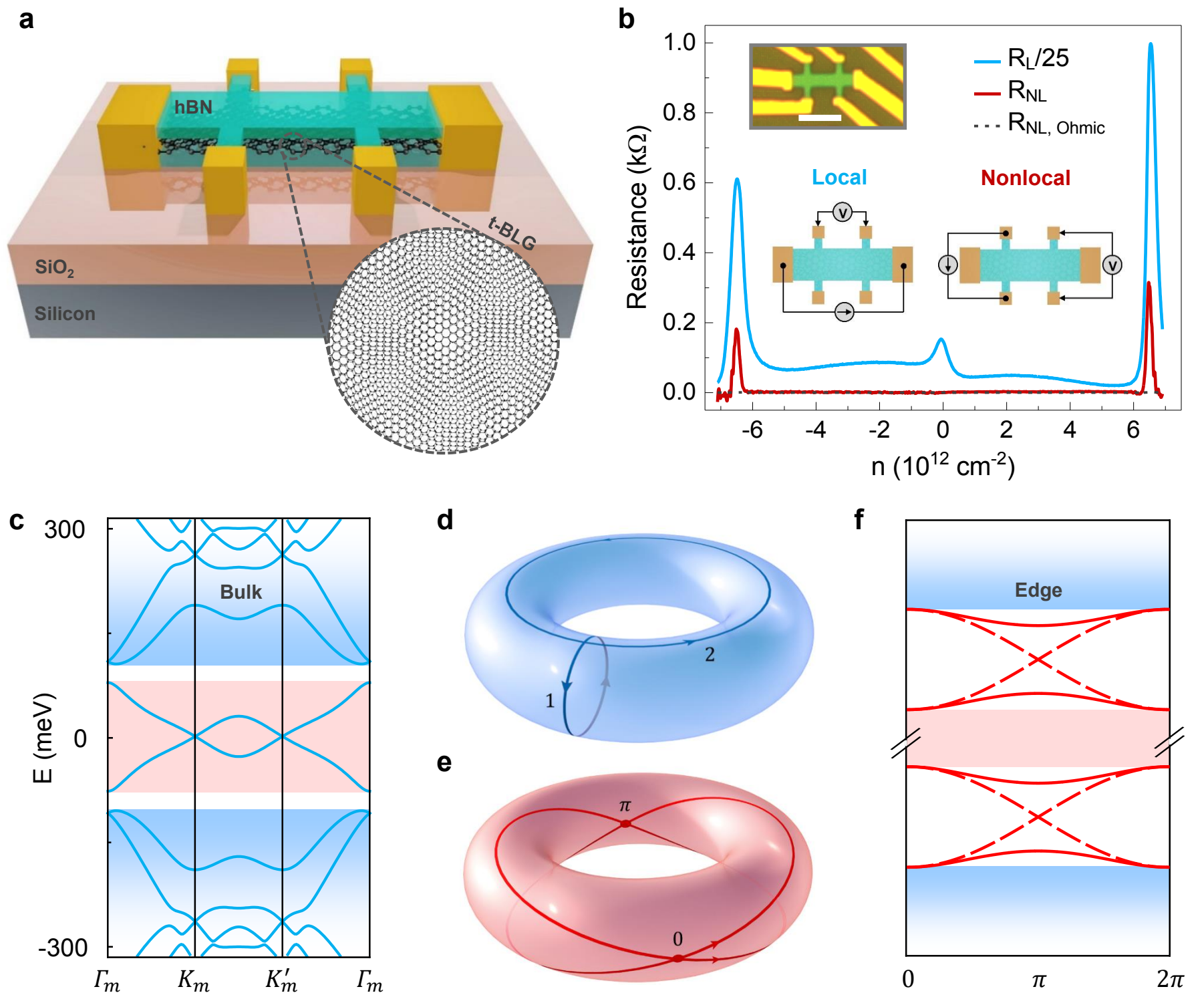


Figure 2: Displacement field dependence of local and nonlocal resistances

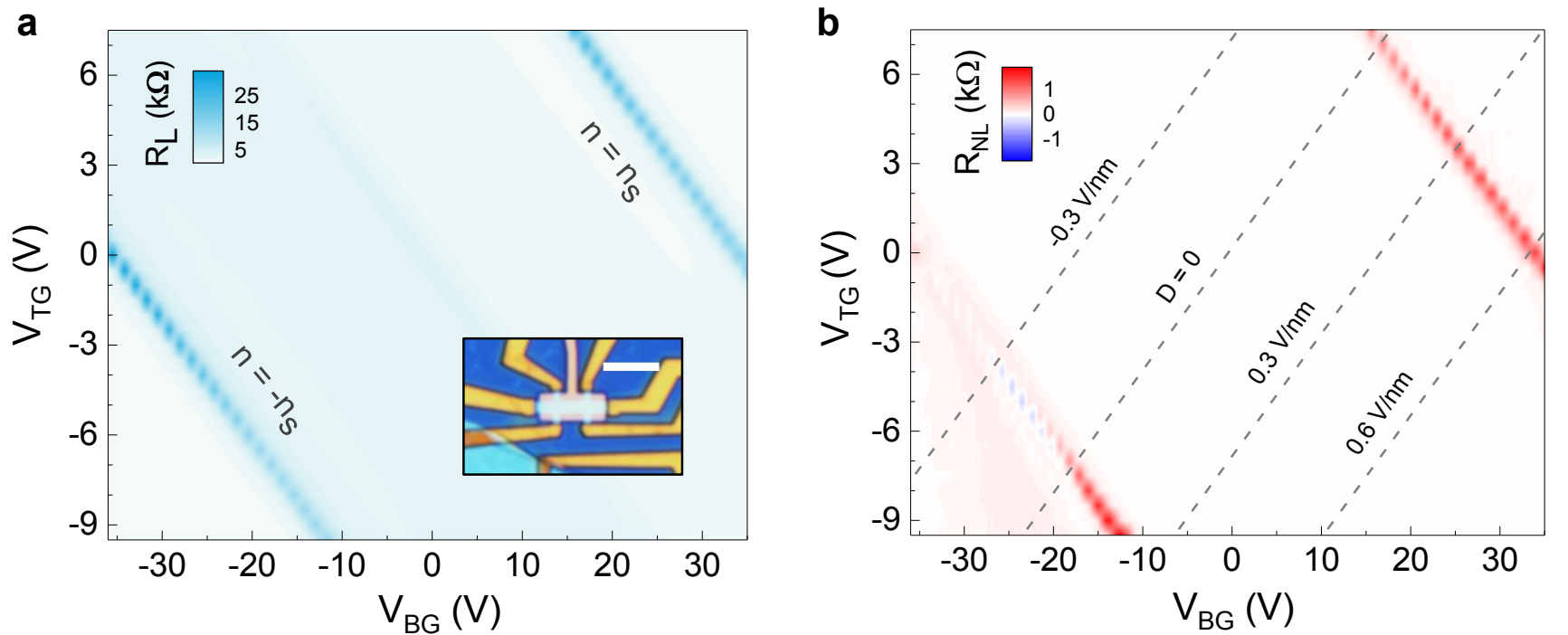


Figure 3: Twist angle dependence of nonlocal resistance and DOS

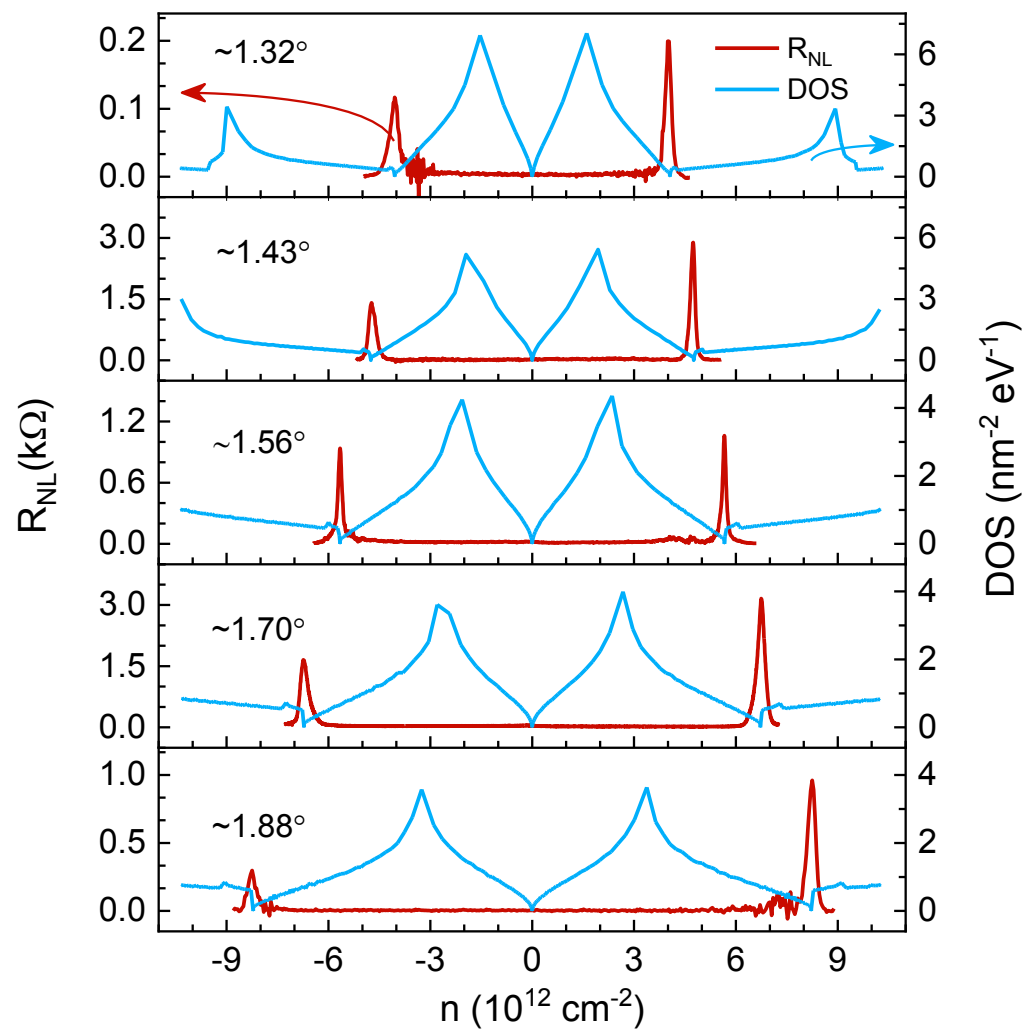


Figure 4: Length and temperature dependence of nonlocal properties

